International Journal of Solids and Structures 50 (2013) 288–296

Contents lists available at SciVerse ScienceDirect

International Journal of Solids and Structures

journal homepage: www.elsevier.com/locate/ijsolstr

A point collocation method for geometrically nonlinear membranes

Kyle F. Kolsti *, Donald L. Kunz

Air Force Institute of Technology, Department of Aeronautics & Astronautics, Wright-Patterson AFB, OH 45433, United States

ARTICLE INFO

Article history:
Received 19 March 2012
Received in revised form 9 July 2012
Available online 7 September 2012

Keywords:
Membrane
Nonlinear
Collocation
Validation

ABSTRACT

This paper describes the development of a numerical model for geometrically nonlinear membranes and evaluates its performance for membranes at static equilibrium. The scheme has several features not commonly seen in structural finite element analysis: the point collocation method, group formulation, and a staggered mesh. In the point collocation finite element method, the partial differential equations are solved at each node instead of by integrating over elements. The group formulation simplifies the handling of nonlinearities by interpolating the nonlinear products of variables, as opposed to seeking the product of independently interpolated variables. The domain is discretized with a staggered mesh of linear triangles and associated polygons. Two sequential gradient recovery operations are performed: first the gradients of the linear triangles are calculated and converted to stresses; then, polygon derivative shape functions derived in this paper are used to determine the internal forces from the stress gradients. The resulting system of nonlinear equations is solved with a Jacobian-free Newton–Krylov solver. The code is first verified using the patch test and the method of manufactured solutions. Then the results are validated using experimental data and benchmark code results in the literature for the Hencky problem (a circular membrane with a fixed perimeter and uniform inflation pressure). The observed rates of convergence for both displacement and radial strain were two. For the configurations and grids used in this investigation, the scheme was suitable for accurately predicting sub-hyperelastic deformations.

Published by Elsevier Ltd.

1. Introduction

Micro Air Vehicles often utilize flapping wings with membranes as the lifting surfaces. Supported by a frame, the membrane's passive response to aerodynamic loads can improve gust response (Lian et al., 2003) and stall characteristics (Shyy et al., 2005). Experimental examination of a fixed membrane wing indicated the membrane oscillations strongly interacted with the separated shear layer and vortex shedding, with up to five vibration modes observed (Rojratsirikul et al., 2009). High-fidelity numerical simulations of a similar configuration with a one-dimensional chordwise structural model realized both standing and traveling wave responses depending upon the flow regime; it was concluded by the authors that an advanced multidisciplinary approach was necessary to fully grasp the complicated system (Gordnier, 2009). The improved insight gained by such efforts will improve design optimization and lead to superior performance. The contribution of this paper is a two-dimensional, highly modular, geometrically nonlinear membrane model, that when interactively coupled with an aerodynamic model will accurately and efficiently predict the membrane response.

Membranes are inherently nonlinear structures that undergo large rigid body displacements and rotations, and often large strains as well. Thorough discussions of membrane mechanics and challenges may be found in Jenkins and Leonard (1991), Jenkins (1996), Pai and Young (2003) and Pai (2007). The prototypical problem for static membrane study is the circular membrane with fixed circumference that is inflated under constant pressure. Commonly called the Hencky problem (Hencky, 1915), this configuration facilitates experimental investigation and permits analytical solutions. Analytical derivations commonly formulate the radial and circumferential equilibrium equations using assumed functions for the dependent variables and solve for the constant coefficients (Liu et al., 1993; Fichter, 1997). Finite element (FE) models have been applied to the Hencky problem using detailed geometric surface descriptions with Jaumann strains and stresses (Pai and Young, 2003). Others have utilized simple linear-elastic elements applicable to the large displacement/small strain regime (Pauletti et al., 2005). In numerical simulations the membrane behavior may be modeled as linear, geometrically nonlinear, or hyperelastic, in order of increasing complexity. The suitability of each of these models is problem-dependent and is affected by the desired ranges of external pressure and membrane prestress (Stanford and Ifju, 2008). Based on those findings and a review of typical Micro Air Vehicle wing designs, a geometrically nonlinear model was selected for the present study. The validation section

* Corresponding author.
E-mail address: kyle.kolsti@wpafb.af.mil (K.F. Kolsti).

0020-7683/$ - see front matter Published by Elsevier Ltd.
http://dx.doi.org/10.1016/j.ijsolstr.2012.08.025

Nomenclature

a	constant coefficient of x for the equation of a polygon side
b	constant coefficient of y for the equation of a polygon side
E	Young's Modulus
$\mathbf{E}$	Green strain
$\mathbf{f}$	normal external force vector
$\mathbf{g}$	surface tangent vector
h	membrane thickness
h^e	representative element length
J_A	membrane area ratio (deformed/original)
J_h	membrane thickness ratio (deformed/original)
κ	weighting coefficient for polygon shape functions
l	linear formula for a side of a polygon
$\hat{\mathbf{n}}$	membrane unit normal vector
$\mathbf{N}$	second Piola–Kirchoff stress per unit length
N_i	polygon shape function for the polygon's vertex node i
p	isotropic inflation pressure or order of convergence (specified in the text)
q	non-dimensional inflation pressure
$\mathbf{Q}$	vector of grouped degrees of freedom at a triangle centroid
R	membrane outer radius
$\mathbf{R}$	residual vector
$\mathbf{T}_\alpha^{Qn}$	matrix partial derivative operator; obtains polygon node values of $\partial\mathbf{Q}/\partial x_\alpha$
$\mathbf{T}_\alpha^{uc}$	matrix partial derivative operator; obtains triangle centroid values of $\partial\mathbf{u}/\partial x_\alpha$
$\mathbf{T}_\alpha^{un}$	matrix partial derivative operator; obtains polygon node values of $\partial\mathbf{u}/\partial x_\alpha$
$\mathbf{u}$	nodal displacement
w	transverse displacement (conventional label for $\mathbf{u}_3$)
x_1, x_2	Cartesian coordinates
x, y	Cartesian coordinates (used in polygon shape function development; same as x_1, x_2)
ϵ	relative error of approximate solution
ν	Poisson ratio
ϕ	dependent variable of interest; specified as displacement or strain as appropriate
ψ	numerator polynomial of a polygon shape function

of this paper will utilize the experimental data from Stanford and Ifju (2008) to establish the model's suitability up to the onset of hyperelastic effects, which occurs at a center deflection of approximately 25% of the circular membrane's radius (Pujara and Lardner, 1978).

The model developed here will utilize two approaches which are relatively rare in structural finite element method (FEM) applications: the point collocation method and the group FE formulation. Both approaches were selected for this effort because they tend to result in simpler formulations (Christie et al., 1981; Zienkiewicz et al., 2005), potentially offering greater code flexibility without sacrificing accuracy. Coincidentally, both the point collocation method and group FE formulation have close ties with the development of computational fluid dynamics (CFD) schemes. Development of the group FE formulation in the literature centers around fluid mechanics applications and examples (Christie et al., 1981; Fletcher, 1983; Fletcher and Srinivas, 1985), and the similar lumping of nonlinear terms in the flux vector is standard practice for finite volume formulations (Hirsch, 2007). Similarly, the point collocation method shares a history with and bears a resemblance to the finite difference method (Zienkiewicz et al., 2005). The nonlinear wave equations that describe membrane dynamics offer an interesting test case for further examining how well these CFD-associated techniques transfer into the structural dynamics milieu.

The collocation method is commonly mentioned in the finite element literature when listing the members of the Method of Weighted Residuals family. However, it is rarely seen in practice. The weighting function for each designated point in the domain is the Dirac delta function. By definition, the Dirac delta function equals zero everywhere except at its associated point, and its integral over the domain equals one (Zienkiewicz et al., 2005). The resulting system of equations solve the PDE (Partial Differential Equation) point-wise rather than in an integral sense. Thus, there is no need for Gaussian integration over an element. Posed in the strong form, the method requires the interpolation scheme to be differentiable to the same order as the PDE (Zienkiewicz et al., 2005; Aluru, 2000), but the formulation of the system of equations has been found to be less complicated than when employing the Galerkin method (Aluru, 2000).

Also, while certainly applicable to a conventional FEM mesh, the point collocation method lends itself to a variety of unconventional discretization and interpolation schemes. Element shapes can expand beyond triangles and quadrilaterals to n-sided polygons. Taking the concept even further, "meshless" (Belytschko et al., 1996; Idelsohn et al., 2003) and "element-free" (Belytschko et al., 1994; Krysl and Belytschko, 1996) methods use least-squares fits, radial basis functions, or other neighboring-node-based techniques for forming the system of equations. Using a meshless point collocation method, Aluru (2000) solve a wide variety of problems including heat conduction, Couette flow, and a cantilever beam. In the interest of computational efficiency for the dynamic simulation, the present model utilizes a staggered background mesh so it does not fall into the meshless category.

In a group finite element formulation (also called "product approximation" (Christie et al., 1981)), aggregated nonlinear terms are first computed, then interpolated as a single degree of freedom. Consider the term $\rho u v$ where ρ, u, and v are each dependent variables (Fletcher and Srinivas, 1985). Rather than applying trial solutions ϕ_j to each of the variables, the group formulation interpolates their precomputed products as $\sum \phi_j (\rho u v)_j$. Significant computational savings have been observed, with the benefits increasing from higher dimensionality or order of nonlinearity (Fletcher, 1983). For some cases, point-wise accuracy may actually be higher than that of the Bubnov–Galerkin method (Christie et al., 1981). This observation hints at a potential synergy in the pairing of the group FE formulation with the point collocation method.

In this paper a novel membrane model using the group finite element formulation and point collocation method will be presented and evaluated for static membranes. After summarizing the governing equations and the material model, polygon interpolation formulas will be derived to calculate gradients in a staggered grid approach. The steps for calculating nodal force imbalances will be described in detail. After the model is explained, verification will demonstrate consistency and an observed rate of convergence of two. Finally, predictions will be validated against experimental results in the literature to show the model to be suitable through its range of intended use (i.e., short of the onset of hyperelastic material response).

2. Governing equations

For this study, a membrane is defined as a thin plate without bending stiffness (Jenkins, 1996). The governing partial differential

equations (PDEs) for the nonlinear membrane are those of a plate undergoing finite deformations as derived in Reddy (1999), but with the moment and curvature terms removed. The internal stress components are N (second Piola–Kirchoff, per unit length) with the subscripts denoting orientation with respect to the Cartesian axis directions x_1 and x_2. The external pressure vector components are represented by f. The terms are expressed in force per unit area.

$$0 = \frac{\partial N_{11}}{\partial x_1} + \frac{\partial N_{12}}{\partial x_2} + f_1 \tag{1}$$

$$0 = \frac{\partial N_{22}}{\partial x_2} + \frac{\partial N_{12}}{\partial x_1} + f_2 \tag{2}$$

$$0 = \frac{\partial}{\partial x_1}\left(N_{11}\frac{\partial u_3}{\partial x_1} + N_{12}\frac{\partial u_3}{\partial x_2}\right) + \frac{\partial}{\partial x_2}\left(N_{22}\frac{\partial u_3}{\partial x_2} + N_{12}\frac{\partial u_3}{\partial x_1}\right) + f_3 \tag{3}$$

The solution of the membrane surface displacements $\mathbf{u}$ begins by recovery of the surface gradients. The gradients then lead to the Green strain tensor components (Reddy, 1999; Bonet and Wood, 1997).

$$\begin{aligned} E_{11} &= \frac{\partial u_1}{\partial x_1} + \frac{1}{2}\left[\left(\frac{\partial u_1}{\partial x_1}\right)^2 + \left(\frac{\partial u_2}{\partial x_1}\right)^2 + \left(\frac{\partial u_3}{\partial x_1}\right)^2\right] \\ E_{22} &= \frac{\partial u_2}{\partial x_2} + \frac{1}{2}\left[\left(\frac{\partial u_1}{\partial x_2}\right)^2 + \left(\frac{\partial u_2}{\partial x_2}\right)^2 + \left(\frac{\partial u_3}{\partial x_2}\right)^2\right] \\ E_{12} &= \frac{1}{2}\left[\frac{\partial u_2}{\partial x_1} + \frac{\partial u_1}{\partial x_2} + \left(\frac{\partial u_1}{\partial x_1}\frac{\partial u_1}{\partial x_2}\right) + \left(\frac{\partial u_2}{\partial x_1}\frac{\partial u_2}{\partial x_2}\right) + \left(\frac{\partial u_3}{\partial x_1}\frac{\partial u_3}{\partial x_2}\right)\right] \end{aligned} \tag{4}$$

The internal stresses are calculated using the conventional plane stress constitutive relationship. Prestress is accounted for by the vector $\mathbf{N}_0$. Note that the membrane thickness $h(\mathbf{u})$ is a function of the displacement field to take thinning into account as the membrane stretches.

$$\begin{Bmatrix} N_{11} \\ N_{22} \\ N_{12} \end{Bmatrix} = \frac{Eh(\mathbf{u})}{1-\nu^2}\begin{bmatrix} 1 & \nu & 0 \\ \nu & 1 & 0 \\ 0 & 0 & (1-\nu)/2 \end{bmatrix}\begin{Bmatrix} E_{11} \\ E_{22} \\ 2E_{12} \end{Bmatrix} + \begin{Bmatrix} N_{11} \\ N_{22} \\ N_{12} \end{Bmatrix}_0 \tag{5}$$

3. Discretization and polygon interpolation formulas

By using the group formulation, all three governing PDEs (Eqs. (1)–(3)) were cast into the same first-order PDE form

$$\frac{\partial \mathbf{Q}_1}{\partial x_1} + \frac{\partial \mathbf{Q}_2}{\partial x_2} + \mathbf{f} = 0 \tag{6}$$

where the vectors $\mathbf{Q}$ define the degrees of freedom as

$$\mathbf{Q}_1 = \begin{Bmatrix} N_{11} \\ N_{12} \\ N_{11}\frac{\partial u_3}{\partial x_1} + N_{12}\frac{\partial u_3}{\partial x_2} \end{Bmatrix} \quad \mathbf{Q}_2 = \begin{Bmatrix} N_{12} \\ N_{22} \\ N_{22}\frac{\partial u_3}{\partial x_2} + N_{12}\frac{\partial u_3}{\partial x_1} \end{Bmatrix} \tag{7}$$

The domain is discretized by forming a staggered mesh, meaning different variables are evaluated at different points in the domain. For example, the displacements u and the stresses N will not be computed at the same nodes. As commonly found in finite difference discretizations, a staggered mesh enables more compact stencils. In certain CFD applications, high-frequency oscillations are reduced because the pressure and velocity fields are fully coupled (Hirsch, 2007).

The staggered mesh consists of a primary mesh of three-node linear triangles and a dual mesh of polygons. The nodes of the primary mesh define the model's collocation points and carry the vectors $\mathbf{u}$ (displacement) and $\mathbf{f}$ (external force). The role of the primary mesh is to recover the first partial derivatives of the membrane surface. The calculated partials of each triangle are placed at the centroid, as is common in post-processing gradient recovery procedures (Cook et al., 2002; Zienkiewicz et al., 2005; Payen and Bathe, 2011).

The dual mesh is formed by connecting the centroids of the triangles to form vertex-centered polygons, also called tributary areas (Zienkiewicz et al., 2005). Note that the polygons do not overlap and are therefore not the same as an element patch. The vertices of the polygons carry the $\mathbf{Q}$ vectors. The solution of the discretized governing equations, Eq. (6), requires an approximation of the partial derivatives of $\mathbf{Q}$ at the center node. For this study, the polygon patch interpolation presented in Dasgupta (2003) was used. This interpolation is based on the linear interpolation along the edge between adjacent nodes. The shape functions are rational polynomials that interpolate a linear field exactly. For completeness, we first list a few key equations from Dasgupta (2003), and then derive the necessary partial derivatives of the shape functions.

Let n be the number of vertices of the polygon and i be an index of those n sides. To use the subscripts to indicate the pertinent node, the coordinates (x_1, x_2) used so far will be renamed (x, y) in this section. Each edge segment l is described by a line with constant coefficients a and b.

$$l_i = 1 - a_i x - b_i y \tag{8}$$

Each polygon will have the center node as its local origin. The coefficients a and b are then determined by the vertex coordinates in the reference configuration.

$$\begin{aligned} a_i &= \frac{y_i - y_{i-1}}{x_{i-1}y_i - x_i y_{i-1}} \\ b_i &= \frac{x_{i-1} - x_i}{x_{i-1}y_i - x_i y_{i-1}} \end{aligned} \tag{9}$$

The line coefficients a and b and the vertex coordinates are used to calculate the relative weight coefficients κ, which are normalized by setting κ_1 to a value of one.

$$\kappa_i = \kappa_{i-1}\left[\frac{a_{i+1}(x_{i-1} - x_i) + b_{i+1}(y_{i-1} - y_i)}{a_{i-1}(x_i - x_{i-1}) + b_{i-1}(y_i - y_{i-1})}\right]; \quad \kappa_1 = 1 \tag{10}$$

The line equations and coefficients form the terms of ψ_i, the numerator of the shape function associated with perimeter node i.

$$\psi_i(x,y) = \kappa_i \prod_{\substack{j=n \\ j\neq i \\ j\neq i+1}} l_j(x,y) \tag{11}$$

The denominator polynomial is equal to the sum of all of the numerator polynomials, thus forming the rational polynomial shape function N_i for each node i on the perimeter of the polygon.

$$N_i(x,y) = \frac{\psi_i}{\sum_{j=1}^{n}\psi_j} \tag{12}$$

Having summarized the work of Dasgupta (2003), we now obtain the derivatives of the shape functions for use in the present method. Application of the quotient rule leads to the expressions for the shape function derivatives,

$$\frac{\partial N_i}{\partial x}(x,y) = \frac{\left(\sum_{j=1}^{n}\psi_j\right)\frac{\partial \psi_i}{\partial x} - \psi_i \frac{\partial}{\partial x}\left(\sum_{j=1}^{n}\psi_j\right)}{\left(\sum_{j=1}^{n}\psi_j\right)^2} \tag{13}$$

$$\frac{\partial N_i}{\partial y}(x,y) = \frac{\left(\sum_{j=1}^{n}\psi_j\right)\frac{\partial \psi_i}{\partial y} - \psi_i \frac{\partial}{\partial y}\left(\sum_{j=1}^{n}\psi_j\right)}{\left(\sum_{j=1}^{n}\psi_j\right)^2} \tag{14}$$

Each of the terms necessary for this calculation will now be simplified. Multiple applications of the chain rule to Eq. (11) result in the expressions

$$\frac{\partial \psi_i}{\partial x} = \kappa_i \sum_{\substack{k\neq i \\ k\neq i+1}}^{k=n} \left(\frac{\partial l_k}{\partial x} \prod_{\substack{j\neq i \\ j\neq i+1 \\ j\neq k}}^{j=n} l_j \right) \tag{15}$$

$$\frac{\partial \psi_i}{\partial y} = \kappa_i \sum_{\substack{k\neq i \\ k\neq i+1}}^{k=n} \left(\frac{\partial l_k}{\partial y} \prod_{\substack{j\neq i \\ j\neq i+1 \\ j\neq k}}^{j=n} l_j \right) \tag{16}$$

The partial derivatives of the linear edge functions are constants,

$$\begin{aligned} \frac{\partial l_i}{\partial x} &= -a_i \\ \frac{\partial l_i}{\partial y} &= -b_i \end{aligned} \tag{17}$$

which when substituted into Eqs. (15) and (16) reduce them to

$$\begin{aligned} \frac{\partial \psi_i}{\partial x} &= -\kappa_i \sum_{\substack{k\neq i \\ k\neq i+1}}^{k=n} \left(a_k \prod_{\substack{j\neq i \\ j\neq i+1 \\ j\neq k}}^{j=n} l_j \right) \\ \frac{\partial \psi_i}{\partial y} &= -\kappa_i \sum_{\substack{k\neq i \\ k\neq i+1}}^{k=n} \left(b_k \prod_{\substack{j\neq i \\ j\neq i+1 \\ j\neq k}}^{j=n} l_j \right) \end{aligned} \tag{18}$$

Since the local origin was placed at the center node, and the center node is the only point at which this interpolation will be applied, all of the non-constant terms of the derivative shape functions can be disregarded. Then the calculations for the individual terms of Eqs. (13) and (14) reduce to

$$\psi_i = \kappa_i \tag{19}$$

$$\sum\nolimits_{j=1}^{n} \psi_j = \sum_{j=1}^{n} \kappa_j \tag{20}$$

$$\frac{\partial \psi_i}{\partial x} = -\kappa_i \sum_{\substack{k\neq i \\ k\neq i+1}}^{k=n} a_k \tag{21}$$

$$\frac{\partial \psi_i}{\partial y} = -\kappa_i \sum_{\substack{k\neq i \\ k\neq i+1}}^{k=n} b_k \tag{22}$$

$$\frac{\partial}{\partial x}\left(\sum_{j=1}^{n} \psi_j \right) = \sum_{j=1}^{n} \frac{\partial \psi_j}{\partial x} \tag{23}$$

$$\frac{\partial}{\partial y}\left(\sum_{j=1}^{n} \psi_j \right) = \sum_{j=1}^{n} \frac{\partial \psi_j}{\partial y} \tag{24}$$

These formulas are substituted into Eqs. (13) and (14) to provide the derivatives of the polygonal shape functions at the center nodes. Thus letting Q_i be scalar values at the polygon vertices $i = 1 \ldots n$, the partial derivatives of Q at the polygon's center node are

$$\frac{\partial Q}{\partial x} = \sum_{i=1}^{n} \frac{\partial N_i}{\partial x} Q_i \tag{25}$$

$$\frac{\partial Q}{\partial y} = \sum_{i=1}^{n} \frac{\partial N_i}{\partial y} Q_i \tag{26}$$

To improve computational efficiency, much like global stiffness matrices, the individual element interpolation functions are assembled into global derivative matrices $\mathbf{T}_\alpha \equiv \partial/\partial x_\alpha$, where $\alpha = 1, 2$ to indicate the direction of the partial derivative. To distinguish between the sets of matrices, let the superscripts indicate the vector upon which the matrix operates ($\mathbf{u}$ or $\mathbf{Q}$) and the location of the result (c for triangle centroid or n for the interior node of a polygon). The derivative matrices $\mathbf{T}_\alpha^{uc}$ recover the linear triangle partial derivatives from the nodal displacements. The equations for the gradients of linear triangles may be found in most introductory finite element texts. The derivative matrices $\mathbf{T}_\alpha^{un}$ use the polygon interpolations to recover the partial derivatives of $\mathbf{u}$ at the polygon interior nodes from the displacements at the perimeter nodes. Lastly, $\mathbf{T}_\alpha^{Qn}$ use the polygon interpolations to recover the partial derivatives of $\mathbf{Q}$ at the polygon interior nodes from the values $\mathbf{Q}$ at the triangle centroids.

4. Residual calculations

The residual vector $\mathbf{R}$ contains the imbalance between the internal and external forces at the nodes for an approximate solution of the governing equations, Eq. (6). The role of the solver is to reduce the size of the residual vector to an acceptable level with the user supplying the metric and tolerance. Using the entire domain, let n_e be the number of triangular elements, n be the total number of nodes, and n_n be the number of interior nodes. The following quantities are calculated sequentially to return the residual vector $\mathbf{R}$ to the solver.

1. Partial derivatives of $\mathbf{u}$ at the triangle centroids using the primal mesh. Six operations are required (partials of three $\mathbf{u}$ vectors in two directions) using the two pre-calculated discrete derivative operators $\mathbf{T}^{uc}$.

$$\frac{\partial \mathbf{u}_i}{\partial x_\alpha} = \mathbf{T}_\alpha^{uc} \mathbf{u}_i, \quad \alpha = 1, 2, \quad i = 1, 2, 3 \tag{27}$$

2. Surface unit normal vector $\hat{\mathbf{n}}$ and area ratio J_A at the center nodes. The surface normals at the nodes were obtained via the cross-product of two tangent vectors (Wriggers, 2008; Bonet and Wood, 1997). The nodal partial derivatives required by the tangent vectors can be obtained by gradient recovery techniques or by applying the polygon interpolation Eqs. (13) and (14) to the full element patch. The latter technique was applied using the two pre-calculated constant matrices $\mathbf{T}^{un}$ in six operations,

$$\frac{\partial \mathbf{u}_i}{\partial x_\alpha} = \mathbf{T}_\alpha^{un} \mathbf{u}_i \quad \alpha = 1, 2, \quad i = 1, 2, 3 \tag{28}$$

Thus at each interior node the tangent vectors were

$$\begin{aligned} \mathbf{g}_1 &= \left\{ 1 + \frac{\partial u_1}{\partial x_1}, \frac{\partial u_2}{\partial x_1}, \frac{\partial u_3}{\partial x_1} \right\}^T \\ \mathbf{g}_2 &= \left\{ \frac{\partial u_1}{\partial x_2}, 1 + \frac{\partial u_2}{\partial x_2}, \frac{\partial u_3}{\partial x_2} \right\}^T \end{aligned} \tag{29}$$

Their cross product's magnitude, J_A, is the ratio of the deformed area to the undeformed area. The direction provides the components of the external force vector. The unit normal vector is

$$\hat{\mathbf{n}} = \frac{\mathbf{g}_1 \times \mathbf{g}_2}{\|\mathbf{g}_1 \times \mathbf{g}_2\|} = \frac{\mathbf{g}_1 \times \mathbf{g}_2}{J_A} \tag{30}$$

3. External force $\mathbf{f}(\mathbf{u})$ at the center nodes. Let p be the spatially-constant magnitude of inflation pressure that acts normal to the membrane in its current configuration. The external force vector is

$$\mathbf{f} = p J_A \hat{\mathbf{n}} \tag{31}$$

4. Thickness ratio J_h at the center nodes. Incompressibility is assumed for the deformed thickness calculation. Since the volume $V = Ah$ is constant, the thickness ratio J_h is the reciprocal of the area ratio.

$$J_h = \frac{h}{h_0} = \frac{V/A}{V/A_0} = \frac{A_0}{A} = \frac{1}{J_A} \tag{32}$$

5. $\mathbf{Q}_1$ and $\mathbf{Q}_2$ at the triangle centroids using Eqs. (4), (5), and (7). The deformed thickness $h(\mathbf{u})$ in Eq. (5) will need to be replaced by $J_h h_0$. Since J_h will be calculated at the center node, not at the element centroids where $\mathbf{Q}$ exists, the undeformed membrane thickness h_0 is used for now. The membrane thickness will be corrected in the last step, when the residual vector is calculated.
6. Partial derivatives of $\mathbf{Q}_1$ and $\mathbf{Q}_2$ at the polygons' center nodes by applying the two pre-calculated derivative operators $\mathbf{T}^{Qn}$ to the three $\mathbf{u}$ vectors.

$$\frac{\partial \mathbf{Q}_\beta}{\partial x_\alpha} = \mathbf{T}^{Qn}_\alpha \mathbf{Q}_\beta, \quad \alpha, \beta = 1, 2 \tag{33}$$

7. Global residual vector $\mathbf{R}$. The nodal thickness ratio J_h from Eq. (32) is now applied to the partial derivatives of $\mathbf{Q}$ to calculate $\mathbf{R}_j \in \Re^3$, residual vector of node j. The nodal residuals are assembled into the global residual vector $\mathbf{R} \in \Re^{3n_n}$, which is returned to the nonlinear solver for further minimization.

$$\mathbf{R}_j = \left(J_h \frac{\partial \mathbf{Q}_1}{\partial x_1} + J_h \frac{\partial \mathbf{Q}_2}{\partial x_2} + \mathbf{f} \right)_j \quad j = 1 \ldots n_n \tag{34}$$

In the point collocation method, the residual equations for points on the boundary are determined by the boundary conditions and will be different from the domain interior's governing equation (Aluru, 2000). Here, for the homogeneous boundary conditions, the displacements are simply set to zero, and the boundary nodes are removed from the solution vector.

5. Nonlinear solver selection

The dynamic simulation under development which will use this membrane model primarily employs an accelerated fixed-point iteration algorithm. This method does not require the construction of a Jacobian matrix (or even an approximation of one), so significant savings in computational effort are expected. Since the Newton–Raphson method will not be used, the tangent stiffness matrix is not needed and will not be formulated analytically. Thus for the static cases presented here it was necessary to find an efficient alternative method that estimates the Jacobian or avoids using it altogether.

For this study we utilized "`family scipy.optimize.newton_krylov`", the Newton–Krylov nonlinear equation solver from the Python library SciPy (Jones et al., 2001). The solver was supplied an initial guess for $\mathbf{u}$ and a callable function that returned the residual vector $\mathbf{R}(\mathbf{u})$, Eq. (34). The loose generalized minimum residual (LGMRES) method was selected as the inner solver (Baker et al., 2005).

Broadly speaking, Newton–Krylov methods employ nested iterative solvers. The outer solver performs corrections like the classical Newton method. The inner solver is one of many linear Krylov subspace methods (Van der Vorst, 2003). Jacobian-free Newton–Krylov (JFNK) methods like the one used in this SciPy routine are efficient for large systems because they use a perturbation of the entire solution vector to approximate Jacobian-vector products; this approach is more efficient than the finite difference Jacobian construction, which requires a perturbation of each element of the solution vector (Knoll and Keyes, 2004; Kelley, 1995). The actual Jacobian is not needed, yet convergence can approach that of the Newton method. Preconditioning by providing an approximation to the Jacobian is highly recommended and often necessary for adequate performance (Benzi, 2002; Van der Vorst, 2003); however, for the simulations in this study, performance was more than adequate without supplying a preconditioner to the solver.

Because stress stiffening is the source of transverse resistance, the solver will fail when starting from a flat, slack membrane. There are several remedies for this problem. The approach used in this study was to prescribe an initially non-flat shape (Wu et al. (1996) used this approach for a box-shaped membrane and mentioned its necessity). Simple parabolic profiles were sufficient. A second option, dynamic relaxation, uses a dynamic model with damping to settle to the static solution (Jenkins and Leonard, 1991; Cook et al., 2002; Wriggers, 2008). This option is convenient since it is not necessary to code a separate solver for the static solution; and it also has the benefit of verifying some aspects of the dynamic code. However, convergence can be extremely slow if the damping mechanism is not carefully designed. Some of these challenges can be avoided by using pseudo-transient continuation (Gee et al., 2009; Kelley and Keyes, 1998). The non-physical time step sizes can be controlled using the successive evolution-reaction (SER) technique (Knoll and Keyes, 2004). A third approach, also not employed herein, entails applying a pretension initially to aid the solver and later removing it for the final solution.

It is worth mentioning a few other numerical alternatives that may be used in the absence of an analytical Jacobian. A more comprehensive review of these alternatives may be found in Wriggers (2008). Finite difference Jacobian approximations are easy to perform but are not robust, and they become very expensive as the size of the problem increases. Automatic differentiation extracts the derivatives directly from the code (Griewank and Walther, 2008). Multigrid methods (Briggs et al., 2000; Henson, 2003) (in particular the Full Approximation Scheme (Brandt, 1977)), and combinations of Newton–Krylov and multigrid methods (Jones and Woodward, 2001; Gee and Tuminaro, 2006) require some careful coding, but the ultimate computational efficiency gains can be impressive. Lastly, depending upon how the method is formulated, dynamic relaxation may also be a viable alternative.

6. Verification

Patch tests were performed for the linear plane stress scenario (Hughes, 1987). All of the tests featured a unit vertical rigid body translation. The square patch measured two units per side and was centered at $(1, 1)$ as shown in Fig. 1. The patch contained a single interior node at $(1.6, 1.4)$, approximately on the perimeter of its dual-mesh polygon. Given a linear displacement field, boundary nodes were displaced accordingly and the displacement of the center node was checked against the exact field. The physical constants were $E = 1000$, $h = 1$, and $\nu = 0.5$. The results in Table 1

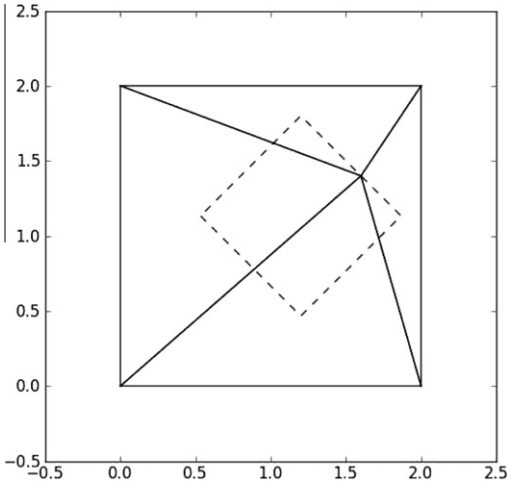

Fig. 1. Square 2×2 5-node patch for the patch test. Solid lines are the triangles of the primary mesh and dashed lines illustrate the node-centered polygon of the dual mesh.

show that the model exactly reproduced the constant strains and stresses, even with irregular elements.

Further verification and convergence determination was performed using the Method of Manufactured Solutions (Roache, 1998; Burg et al., 2004). In this method, a solution is fabricated (it does not have to be physically plausible), and the forcing function is calculated from the governing PDE; then the forcing function is used in the numerical model to obtain an approximate solution. The error is then the difference between the model's solution and the manufactured solution. The manufactured solution, Eq. (35), was devised in accordance with the recommended guidelines found in Salari and Knupp (2000). Non-unity constants were chosen such that the solution magnitudes and derivatives were of approximately the same order of magnitude in all three axes such that potential formula errors might be revealed.

$$\mathbf{u}(x_1, x_2) = \begin{Bmatrix} 0.17e^{(x_1/2 - x_2/2)} \\ -0.37e^{(-x_1/4 - x_2/2)} \\ 0.71e^{(x_1 + x_2)} \end{Bmatrix} \tag{35}$$

Table 1
Patch test results. A star (∗) indicates a non-zero magnitude of less than 10^{-11}; strains and stresses for all four elements were reported as exact when integer values, and exact to at least eight decimal places when fractional.

u field	**u**(1.6,1.4)	**E**	**N**/h
(1,0,1)	(1,0*,1)	(0,0*,0*)	(0*,0*,0*)
(0,1,1)	(0*,1,1)	(0,0*,0*)	(0*,0*,0*)
(x,0,1)	(1.6,0*,1)	(1.5,0*,0)	(2000,1000,0)
(0,x,1)	(0*,1.6,1)	(0.5,0*,0.5)	(666.7,333.3,333.3)
(y,0,1)	(1.4,0*,1)	(0,0.5,0.5)	(333.3,666.7,333.3)
(0,y,1)	(0*,1.4,1)	(0,1.5,0*)	(1000,2000,0*)

The lengthy formulas for the corresponding anisotropic pressure vector were obtained by substituting the manufactured solution **u** of Eq. (35) into Eqs. (1)–(5). This process was performed independently of the point collocation code. The pressure vector formulas were generated symbolically with the Python library SymPy (SymPy Development Team, 2009) and inserted into the point collocation model. The Dirichlet boundary conditions were satisfied by constraining perimeter node displacements in accordance with the manufactured solution, Eq. (35).

To investigate the effects of discretization error, verification was performed on two domains: a hexagon and a circle. The hexagonal domain was ideally discretized with a structured, symmetrical primary mesh of equilateral triangles to minimize discretization error. The six points of the domain laid on the unit circle. The unit-radius circular domain was discretized with asymmetrical, unstructured grids—the same grids which will be used later in the validation phase. Three grids from each domain are shown in Fig. 2. All grids were created using the open source software Gmesh (Geuzaine and Remacle, 2009), which contains a "refine by splitting" feature (elsewhere called "refine by quartering" (Knabner and Angermann, 2003)) to easily perform structured refinement with a grid ratio of two. For this study the representative element size of a mesh, h^e, was calculated as the length of the side of an equilateral triangle, where the area of the triangle was equal to the mean element area. The error measures ϵ_u and ϵ_E were the Euclidean norms of the displacement error vector and the strain error vector at the origin, respectively. The strain was recovered as the mean of the strains of the surrounding triangular elements. Both measures were normalized by the value of the exact solution.

The convergence study results are shown in Table 2 and Fig. 3. The observed order of accuracy p converged to two for both

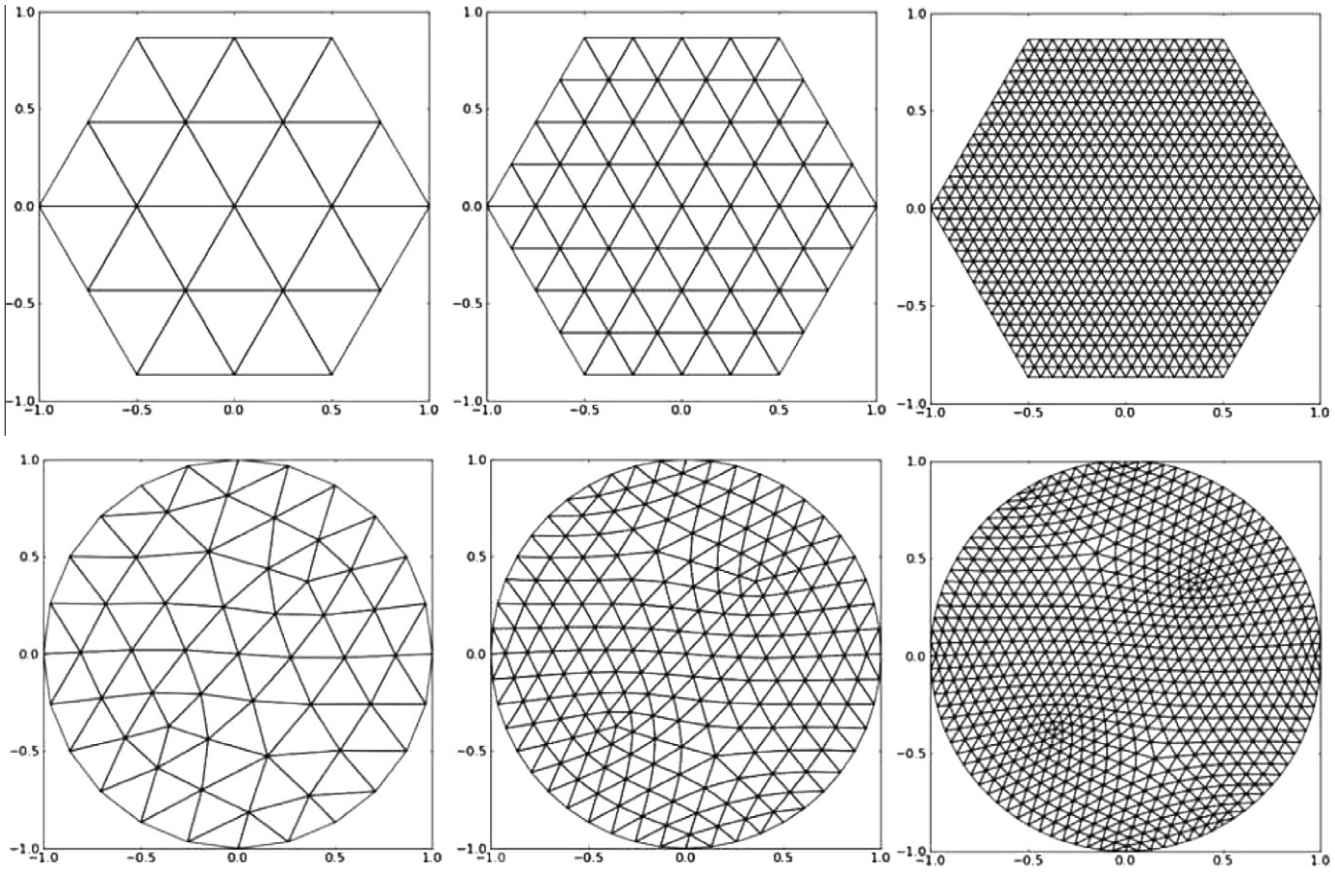

Fig. 2. Top row: hexagonal grids with $h^e = 0.5, 0.25$, and 0.0625 (hex2, hex4, and hex16). Bottom row: the three finest circular grids used for both verification and validation (circle3, circle2, and circle1, left-to-right).

Table 2
Convergence study results. The hexagonal grids are labeled with the number of elements from the origin to the vertex at $(1,0)$. The circular grids are numbered sequentially from fine to coarse.

Grid	h^e	$\log(h^e)$	$\log(\epsilon_u)$	p_u	$\log(\epsilon_E)$	p_E
hex2	0.5	−0.30	−1.04	–	−0.98	–
hex4	0.25	−0.60	−1.74	2.32	−1.75	2.56
hex8	0.125	−0.90	−2.36	2.07	−2.39	2.13
hex16	0.0625	−1.20	−2.97	2.02	−3.00	2.03
hex32	0.03125	−1.51	−3.57	2.00	−3.60	2.01
hex64	0.015625	−1.81	−4.17	2.00	−4.21	2.00
circle4	0.537	−0.27	−0.77	–	−1.02	–
circle3	0.273	−0.56	−1.47	2.39	−2.93	6.50
circle2	0.137	−0.86	−2.10	2.10	−2.80	−0.42
circle1	0.069	−1.16	−2.72	2.05	−3.29	1.63

displacement and strain in the hexagonal domain. The displacement errors were slightly higher for the circular grids due to the discretization error of the unstructured grid; however, the same order of convergence was observed. The strain convergence in the circular grid did not behave as neatly because the individual strain vector components converged differently: E_{11} from above, E_{12} from below, and E_{22} non-monotonically. Thus the vector norm converged non-monotonically. The slope of a least-squares linear fit of the four circular grids' strain errors provided $p = 2.24$, more in line with the other convergence rates. Interestingly, the circular grids produced more accurate strain predictions than the hexagonal grids despite the non-monotonic strain convergence behavior and lower displacement accuracy.

The verification process has demonstrated that the model correctly and consistently solved the coded governing equations. The method's observed order of convergence of both displacement and strain was two. Also, the circular grids introduced an acceptably small amount of discretization error and are therefore suitable for use in the validation phase.

7. Validation

The point collocation model was validated against the experimental and finite element model results in Stanford and Ifju (2008). In that study, a latex rubber sheet was inflated from below, and the displacement field was extracted by optically tracking a random speckling pattern on the membrane surface. Strains were calculated from the displacement field during post-processing. A geometrically nonlinear finite element model was compared to another finite element approximation by Small and Nix (1992), then validated against the experimental data.

Two cases were selected for validation in this paper: one with and the other without uniform prestress. In the case without prestress, model predictions were compared directly to the experimental data. The physical constants were outer radius $R = 57.15$ mm, thickness $h = 0.12$ mm, modulus of elasticity $E = 2$ MPa, and Poisson ratio $\nu = 0.5$.

In the prestressed case, a non-isotropic prestrain field precluded use of the experimental results. The geometrically nonlinear finite element model was therefore used as a benchmark for this study. The FEM model was suitable as a benchmark because it was validated in Stanford and Ifju (2008) against the experimental data for the same problem configuration (including geometry, boundary conditions, material, and load type) and to much greater loads and deformations. The physical constants for this case were $R = 3.5$ mm, $h = 1.0$ μm, $E = 71.0$ GPa, and $\nu = 0.345$. Following convention for the Hencky problem, the lateral deflection is normalized as w/R, and the nondimensional pressure q normalizes the inflation pressure as $q = pR/Eh$.

Representative grid convergence results are shown in Table 3. The format of the presentation comes from Celik et al. (2008), which put forth useful guidelines to standardize the reporting of CFD numerical study results. As explained earlier, all grid ratios are equal to two. The symbol ϕ represents the magnitude of the field variable (displacement or strain). A subscript 1, 2, or 3 indicates the results were obtained from the grid circle1, circle2, or circle3 respectively (see Table 2 and Fig. 3). The calculated order of accuracy is p. The symbol ϕ_{ext}^{32} indicates the value was obtained from Richardson extrapolation using grids 2 and 3. The approximate and extrapolated relative errors (magnitude percentage change in ϕ from one grid to the next finer) are shown as ϵ_a and ϵ_{ext}.

The convergence study confirms that the grids were sufficiently refined, as indicated by the convergence of the extrapolated values ϕ_{ext} and the low relative errors ϵ. The extrapolated values ϕ_{ext}^{21} were taken as the model solution for the remaining discussions. The second-order observed accuracy from the verification phase was maintained for both displacement and strain within the range of the model's expected applicability. The order of convergence of

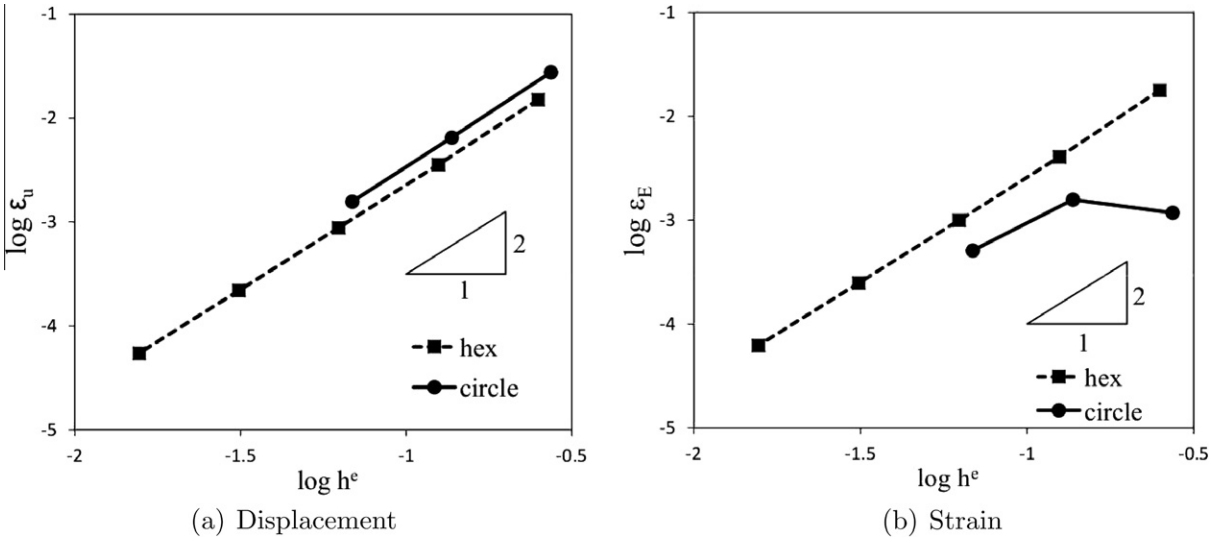

Fig. 3. Convergence study. The triangle displays a reference slope of two. Dashed lines are hexagonal grid results and solid lines are circular mesh results. Grids hex2 and circle4 from Table 2 are omitted.

Table 3
Validation convergence study for displacement (w/R) and radial strain (E_r) at the origin.

Dep. variable ϕ	w/R	w/R	E_r	E_r	w/R
Prestress	None	None	None	None	250 MPa
q	0.024	0.048	0.048	0.083	0.0030
ϕ_3 (coarse mesh)	0.1748	0.2223	0.0339	0.0525	0.08005
ϕ_2 (medium)	0.1739	0.2212	0.0348	0.0541	0.07983
ϕ_1 (fine)	0.1737	0.2210	0.0350	0.0546	0.07978
p	2.00	1.96	2.04	1.98	2.05
ϕ_{ext}^{32}	0.1736	0.2209	0.0350	0.0547	0.07976
ϕ_{ext}^{21}	0.1736	0.2209	0.0350	0.0547	0.07976
ϵ_a^{21}	0.13%	0.12%	0.59%	0.76%	0.07%
ϵ_{ext}^{21}	0.04%	0.04%	0.19%	0.26%	0.02%

w/R deteriorated to below one for large deformations (i.e., for $w/R \gtrsim 0.4$).

The point collocation model predictions are compared to the experimental results in Fig. 4 and to the FEM model benchmark in Fig. 5. Agreement is excellent with and without prestress up to $w/R \approx 0.25$, beyond which the point collocation model begins to underestimate the displacement. This behavior is in agreement with the comparison of Mooney–Rivlin and Hookean material models in Pujara and Lardner (1978), so the gradual loss of accuracy beyond this point may be attributed to the onset of hyperelastic effects. The nodal strain predictions continue to match the experimental data beyond $w/R \approx 0.45$. Just as in the verification phase, the strains are actually more accurate than the displacements. Typically the directly-calculated derived variables (strains and stresses) converge more slowly than the displacements, though post-processing recovery procedures may improve the accuracy (Zienkiewicz et al., 2005; Payen and Bathe, 2011). The staggered mesh of this model uses constant-strain triangles, so nodal strain values must be recovered by one of the gradient recovery procedures. Simple averaging from neighboring elements was sufficient to produce the excellent relative accuracy of strain at the center node.

Validation against the experimental data has shown that the model is accurate for displacements up to $w/R \approx 0.25$, at which point a hyperelastic model would be more appropriate as discussed in Stanford and Ifju (2008).

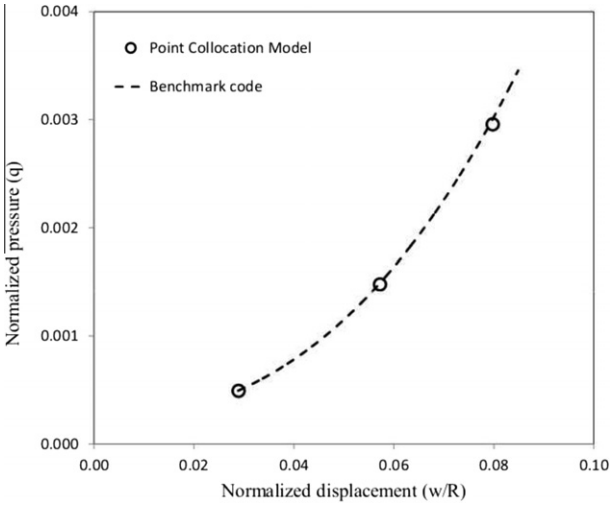

Fig. 5. Validation of the prestressed case by comparison to the FEM benchmark.

8. Conclusions

A membrane model intended for eventual use in dynamic aeroelastic simulations was presented in this paper, and its performance for membranes at static equilibrium was investigated. The model effectively combines several unconventional formulations in structural engineering, including a staggered grid with robust low-order interpolation schemes, grouped nonlinear products as degrees of freedom, and the point collocation method. Method capabilities include variable thickness, follower forces, and arbitrary prestress. Rigorous verification demonstrated consistency, and the observed order of convergence was two for both displacement and strain. During validation with respect to a static circular membrane (the Hencky problem), the point collocation model predictions agreed with experimental data and benchmark FEM code until the region where hyperelastic response began to dominate.

The primary feature that distinguishes this approach is its simplicity. Element integration is avoided entirely. The group formulation permits the same treatment to all three axes, and the resulting code is explicit and self-documenting. Overall, the framework of the approach is highly modular and flexible. Any given step can be performed by interchangeable subroutines. For example, the

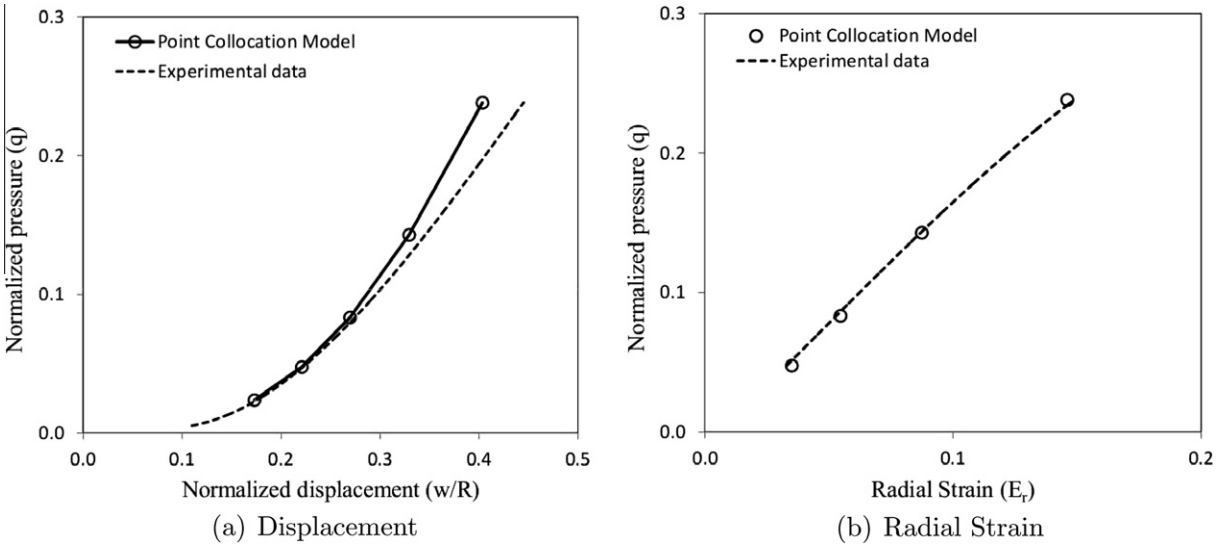

Fig. 4. Validation with no prestress by comparison to experimental data.

polygon interpolation technique could be replaced by least squares or radial basis function routines without upsetting the remaining code. The residual subroutine readily accepts different strain–displacement or material models (including nonlinear models).

Evaluation of the method's suitability for dynamic cases is in progress. As for the scheme itself, further effort is necessary to investigate the sensitivity of the solution to mesh geometry, in particular through analytical *a priori* error estimates and determination of the scheme's order of accuracy. Application to other systems such as hyperelastic membranes and thin plates also offers opportunities for future work.

Acknowledgments

This research was funded by the Air Force Office of Scientific Research Grant No. F1ATA01103J001.

References

Aluru, N.R., 2000. A point collocation method based on reproducing kernel approximations. International Journal for Numerical Methods in Engineering 47 (6), 1083–1121.

Baker, A.H., Jessup, E.R., Manteuffel, T., 2005. A technique for accelerating the convergence of restarted GMRES. SIAM Journal on Matrix Analysis and Applications 26 (4), 962–984.

Belytschko, T., Lu, Y.Y., Gu, L., 1994. Element-free Galerkin methods. International Journal for Numerical Methods in Engineering 37 (2), 229–256.

Belytschko, T., Krongauz, Y., Organ, D., Fleming, M., Krysl, P., 1996. Meshless methods: an overview and recent developments. Computer Methods in Applied Mechanics and Engineering 139 (1–4), 3–47.

Benzi, M., 2002. Preconditioning techniques for large linear systems: a survey. Journal of Computational Physics 182 (2), 418–477.

Bonet, J., Wood, R.D., 1997. Nonlinear Continuum Mechanics for Finite Element Analysis, first ed. Cambridge University Press.

Brandt, A., 1977. Multi-level adaptive solutions to boundary value problems. Mathematics of Computation 31 (138), 333–390.

Briggs, W.L., Henson, V.E., McCormick, S.F., 2000. A Multigrid Tutorial, second ed. Society for Industrial and Applied Mathematics.

Burg, C.O.E., Murali, V.K., June 2004. Efficient code verification using the residual formulation of the method of manufactured solutions. In: AIAA Paper 2004–2628. 34th AIAA Fluid Dynamics Conference. Portland, Oregon.

Celik, I.B., Ghia, U., Roache, P.J., Freitas, C.J., Coleman, H., Raad, P.E., 2008. Procedure for estimation and reporting of uncertainty due to discretization in CFD applications. Journal of Fluids Engineering (Special Publication) 130.

Christie, I., Griffiths, D.F., Mitchell, A.R., Sanz-Serna, J.M., 1981. Product approximation for non-linear problems in the finite element method. IMA Journal of Numerical Analysis 1 (3), 253–266.

Cook, R.D., Malkus, D.S., Plesha, M.E., Witt, R.J., 2002. Concepts and Applications of Finite Element Analysis, fourth ed. John Wiley & Sons, Inc.

Dasgupta, G., 2003. Interpolants within convex polygons: Wachspress' shape functions. Journal of Aerospace Engineering 16 (1), 1–8.

Fichter, W.B., 1997. Some solutions for the large deflections of uniformly loaded circular membranes. NASA Technical Paper 3658, Langley Research Center, Hampton, VA.

Fletcher, C.A.J., 1983. The group finite element formulation. Computer Methods in Applied Mechanics and Engineering 37 (2), 225–244.

Fletcher, C.A.J., Srinivas, K., 1985. Time-split finite element methods in physical and generalized coordinates. In: Gallagher, R.H., Carey, G., Oden, J.T., Zienkiewicz, O.C. (Eds.), Finite Elements in Fluids, Finite Elements and Flow Problems of Wiley Series in Numerical Methods in Engineering, vol. 6. John Wiley & Sons, pp. 115–133 (Chapter 4).

Gee, M.W., Tuminaro, R.S., 2006. Nonlinear algebraic multigrid for constrained solid mechanics problems using Trilinos. Tech. Rep. SAND2006-2256, Sandia National Laboratories.

Gee, M.W., Kelley, C.T., Lehoucq, R.B., 2009. Pseudo-transient continuation for nonlinear transient elasticity. International Journal for Numerical Methods in Engineering 78 (10), 1209–1219.

Geuzaine, C., Remacle, J.-F., 2009. Gmsh: a three-dimensional finite element mesh generator with built-in pre- and post-processing facilities. International Journal for Numerical Methods in Engineering 79 (11), 1309–1331.

Gordnier, R.E., 2009. High fidelity computational simulation of a membrane wing airfoil. Journal of Fluids and Structures 25 (5), 897–917.

Griewank, A., Walther, A., 2008. Evaluating Derivatives: Principles and Techniques of Algorithmic Differentiation, second ed. Society for Industrial and Applied Mathematics.

Hencky, H., 1915. On the stress state in circular plates with vanishing bending stiffness. Zeitschrift für Mathematik und Physik 63 (3), 311–317.

Henson, V.E., 2003. Multigrid methods nonlinear problems: an overview. In: Proceedings of SPIE, vol. 5016, p. 36.

Hirsch, C., 2007. Numerical Computation of Internal & External Flows. John Wiley & Sons, Ltd.

Hughes, T.J.R., 1987. The Finite Element Method. Prentice-Hall, Inc.

Idelsohn, S.R., Oñate, E., Calvo, N., Del Pin, F., 2003. The meshless finite element method. International Journal for Numerical Methods in Engineering 58 (6), 893–912.

Jenkins, C.H., 1996. Nonlinear dynamic response of membranes: state of the art – Update. Applied Mechanics Reviews 10S, S41–S48.

Jenkins, C.H., Leonard, J.W., 1991. Nonlinear dynamic response of membranes: state of the art. Applied Mechanics Reviews 44 (7), 319–328.

Jones, J.E., Woodward, C.S., 2001. Newton–Krylov-multigrid solvers for large-scale, highly heterogeneous, variably saturated flow problems. Advances in Water Resources 24 (7), 763–774.

Jones, E., Oliphant, T., Peterson, P., et al., 2001. SciPy: open source scientific tools for Python. <http://www.scipy.org/>.

Kelley, C.T., 1995. Iterative Methods for Linear and Nonlinear Equations. Society for Industrial and Applied Mathematics.

Kelley, C.T., Keyes, D.E., 1998. Convergence analysis of pseudo-transient continuation. SIAM Journal of Numerical Analysis 35 (2), 508–523.

Knabner, P., Angermann, L., 2003. Numerical Methods for Elliptic and Parabolic Partial Differential Equations, second ed. Springer.

Knoll, D.A., Keyes, D.E., 2004. Jacobian-free Newton–Krylov methods: a survey of approaches and applications. Journal of Computational Physics 193 (2), 357–397.

Krysl, P., Belytschko, T., 1996. Analysis of thin shells by the element-free Galerkin method. International Journal of Solids and Structures 33 (20–22), 3057–3080.

Lian, Y., Shyy, W., Ifju, P.G., Verron, E., 2003. Membrane wing model for micro air vehicles. AIAA Journal 41 (12), 2492–2494.

Liu, S., Haddow, J.B., Dost, S., 1993. A variational approach to a circular hyperelastic membrane problem. Acta Mechanica 99 (1), 191–200.

Pai, P.F., 2007. Highly Flexible Structures: Modeling, Computation, and Experimentation. American Institute of Aeronautics and Astronautics.

Pai, P.F., Young, L.G., 2003. Fully nonlinear modeling and analysis of precision membranes. International Journal of Computational Engineering Science 4 (1), 19–65.

Pauletti, R.M.O., Guirardi, D.M., Deifeld, T.E.C., 2005. Argyris' natural membrane finite element revisited. In: Oñate, E., Kröpling, B. (Eds.), Textile Composites and Inflatable Structures. CIMNE, Barcelona, pp. 335–344.

Payen, D.J., Bathe, K.J., 2011. The use of nodal point forces to improve element stresses. Computers & Structures 89 (5–6), 485–495.

Pujara, P., Lardner, T.J., 1978. Deformations of elastic membranes – Effect of different constitutive relations. Zeitschrift für Angewandte Mathematik und Physik (ZAMP) 29 (2), 315–327.

Reddy, J.N., 1999. Theory and Analysis of Elastic Plates, first ed. Taylor & Francis.

Roache, P.J., 1998. Verification and Validation in Computational Science and Engineering. Hermosa Publishers.

Rojratsirikul, P., Wang, Z., Gursul, I., 2009. Unsteady fluid-structure interactions of membrane airfoils at low Reynolds numbers. Experiments in Fluids 46 (5), 859–872.

Salari, K., Knupp, P., 2000. Code verification by the method of manufactured solutions. Tech. Rep. SAND2000-1444, Sandia National Laboratories.

Shyy, W., Ifju, P., Viieru, D., 2005. Membrane wing-based micro air vehicles. Applied Mechanics Reviews 58 (4), 283–301.

Small, M.K., Nix, W.D., 1992. Analysis of the accuracy of the bulge test in determining the mechanical properties of thin films. Journal of Materials Research 7 (6), 1553–1563.

Stanford, B., Ifju, P., 2008. The validity range of low fidelity structural membrane models. Experimental Mechanics 48 (6), 697–711.

SymPy Development Team, 2009. SymPy: Python library for symbolic mathematics. <http://www.sympy.org>.

Van der Vorst, H.A., 2003. Iterative Krylov Methods for Large Linear Systems, 1st Edition. Cambridge University Press.

Wriggers, P., 2008. Nonlinear Finite Element Methods. Springer.

Wu, B., Du, X., Tan, H., 1996. A three-dimensional FE nonlinear analysis of membranes. Computers & Structures 59 (4), 601–605.

Zienkiewicz, O.C., Taylor, R.L., Zhu, J.Z., 2005. The Finite Element Method: Its Basis and Fundamentals, sixth ed. Butterworth-Heinemann.